Published in final edited form as:
JACC Cardiovasc Imaging. 2017 October ; 10(10 Pt A): 1103–1112. doi:10.1016/j.jcmg.2016.09.029.

Coronary Artery PET/MR Imaging:

Feasibility, Limitations, and Solutions

Philip M. Robson, PhD[a], **Marc R. Dweck, MD, PhD**[a,b], **Maria Giovanna Trivieri, MD**[a,c], **Ronan Abgral, MD**[a,d], **Nicolas A. Karakatsanis, PhD**[a], **Johanna Contreras, MD**[c], **Umesh Gidwani, MD**[c], **Jagat P. Narula, MD, PhD**[c], **Valentin Fuster, MD**[c], **Jason C. Kovacic, MD, PhD**[c], and **Zahi A. Fayad, PhD**[a,c]

[a]Translational and Molecular Imaging Institute, Icahn School of Medicine at Mount Sinai, New York, New York

[b]British Heart Foundation Centre for Cardiovascular Science, University of Edinburgh, Edinburgh, United Kingdom

[c]Cardiovascular Institute, Icahn School of Medicine at Mount Sinai, New York, New York

[d]Department of Nuclear Medicine, University Hospital of Brest, European University of Brittany, EA3878 GETBO, Brest, France.

Abstract

OBJECTIVES—The aims of this study were to describe the authors' initial experience with combined coronary artery positron emission tomographic (PET) and magnetic resonance (MR) imaging using ^{18}F-fluorodeoxyglucose (^{18}F-FDG) and ^{18}F-sodium fluoride (^{18}F-NaF) radiotracers, describe common problems and their solutions, and demonstrate the feasibility of coronary PET/MR imaging in appropriate patients.

BACKGROUND—Recently, PET imaging has been applied to the aortic valve and regions of atherosclerosis. ^{18}F-FDG PET imaging has become established for imaging inflammation in atherosclerosis in the aorta and carotid arteries. Moreover, ^{18}F-NaF has emerged as a novel tracer of active microcalcification in the aortic valve and coronary arteries. Coronary PET imaging remains challenging because of the small caliber of the vessels and their complex motion. Currently, most coronary imaging uses combined PET and computed tomographic imaging, but there is increasing enthusiasm for PET/MR imaging because of its reduced radiation, potential to correct for motion, and the complementary information available from cardiac MR in a single scan.

METHODS—Twenty-three patients with diagnosed or documented risk factors for coronary artery disease underwent either ^{18}F-FDG or ^{18}F-NaF PET/MR imaging. Standard breath-held MR-based attenuation correction was compared with a novel free-breathing approach. The impact on PET image artifacts and the interpretation of vascular uptake were evaluated semiquantitatively by

---

REPRINT REQUESTS AND CORRESPONDENCE: Dr. Philip M. Robson, Icahn School of Medicine at Mount Sinai, TMII 1st Floor, Room 116, 1470 Madison Avenue, New York, New York 10029. philip.robson@mountsinai.org.

The authors have reported that they have no relationships relevant to the contents of this paper to disclose. Nathaniel Reichek, MD, served as the Guest Editor for this paper.

expert readers. Moreover, PET reconstructions with more algorithm iterations were compared visually and by target-to-background ratio.

RESULTS—Image quality was significantly improved by novel free-breathing attenuation correction. Moreover, conspicuity of coronary uptake was improved by increasing the number of algorithm iterations from 3 to 6. Elevated radiotracer uptake could be localized to individual coronary lesions using both ^{18}F-FDG (n = 1, maximal target-to-background ratio = 1.61) and ^{18}F-NaF (n = 7, maximal target-to-background ratio = 1.55 ± 0.37), including in 1 culprit plaque post–myocardial infarction confirmed by myocardial late gadolinium enhancement.

CONCLUSIONS—The authors provide the first demonstration of successful, low-radiation (7.2 mSv) PET/MR imaging of inflammation and microcalcification activity in the coronary arteries. However, this requires specialized approaches tailored to coronary imaging for both attenuation correction and PET reconstruction.

Keywords

atherosclerosis; attenuation correction; coronary imaging; ^{18}F-sodium fluoride; nuclear cardiology; PET/MR imaging

Positron emission tomographic (PET) imaging is an established technology that allows the activity of specific disease processes to be measured in vivo. Cardiac PET imaging is now widely used, primarily to assess myocardial perfusion and viability. More recently, PET imaging has been applied to imaging of the aortic valve (1,2) and regions of atherosclerosis in the vasculature (3). Imaging disease activity in the coronary arteries is challenging because of their small caliber and complex motion (4). Nevertheless recent studies have demonstrated the feasibility of using ^{18}F-fluorodeoxyglucose (^{18}F-FDG) as a marker of plaque inflammation (5) and ^{18}F-sodium fluoride (^{18}F-NaF) as a marker of vascular microcalcification activity in both aortic stenosis and coronary atherosclerosis (6–8).

Traditionally, hybrid PET and computed tomography (CT) platforms are used, with the latter providing both anatomic detail and attenuation correction. The additional radiation doses associated with CT scans have led to considerable interest in novel hybrid systems combining PET cameras and magnetic resonance (MR) scanners (9–11). Moreover, the potential of PET/MR imaging for cardiac applications has been quickly recognized (12–14). However, concerns remain about this new technology, in particular the ability of PET/MR imaging to perform accurate and reliable MR attenuation correction (MRAC) (15).

Here, we report our initial experience with coronary PET/MR imaging using both ^{18}F-FDG and ^{18}F-NaF. We describe common problems and artifacts that were encountered and provide solutions. Ultimately we demonstrate the feasibility of PET/MR imaging in coronary atherosclerosis.

METHODS

PATIENT POPULATION

Patients with either established coronary artery disease, or documented risk factors for coronary artery disease were recruited for PET/MR imaging in 2 cohorts. Cohort 1 was used to gain initial experience to guide technological developments that were to be evaluated in the larger cohort 2. Exclusion criteria were MR-incompatible implants, insulin-dependent diabetes, claustrophobia, and pregnancy or breastfeeding. Our Institutional Review Board approved this study, and all patients gave written informed consent.

PET/MR IMAGING

All imaging was performed on a hybrid simultaneous PET/MR system (Biograph mMR, Siemens Healthcare, Erlangen, Germany). The body transmission coil, a flexible 6-channel body arrayed receiver, and a 6-channel spine arrayed receiver mounted in the scanner table were used to acquire MR data. For attenuation correction of PET data, only the transmit coil and spine array were included in the attenuation map.

For both ^{18}F-NaF and ^{18}F-FDG PET imaging, patients were injected with 5 MBq/kg of tracer (5,7) and then rested in a quiet environment for about 30 min before beginning PET acquisition, which lasted 60 min. For ^{18}F-FDG PET imaging, patients were required to have fasted for at least 6 h and to have serum blood glucose levels <200 mg/dl prior to tracer injection.

PET data were recorded in list-mode format. The initial PET image reconstruction used an iterative ordinary Poisson ordered-subsets expectation maximization algorithm with 21 subsets and 3 iterations incorporating point-spread function resolution modeling (16), a 344 × 344 × 127 matrix, and a 2-mm full-width-at-half-maximum Gaussian post-reconstruction filter. Attenuation correction for the body in the PET reconstruction was estimated using MR imaging (see “Technological Development” section). The MR protocol included: 1) anatomic imaging, long-axis and short-axis cardiac cine images; 2) whole-heart, 3-dimensional, contrast-enhanced, coronary MR angiography using a respiratory-navigated, electrocardiographically triggered, inversion-recovery fast spoiled gradient-echo sequence, using 0.2 mmol/kg Multihance (Bracco, Milan, Italy) (17); and 3) late gadolinium enhancement short-axis images, approximately 10 min post–contrast injection. The MR imaging protocol lasted about 70 min.

TECHNOLOGICAL DEVELOPMENT. MRAC

Standard MRAC of PET data on the Biograph mMR is performed using end-expiration, breath-held, 3-dimensional, dual-echo spoiled gradient-recalled echo (GRE) acquisitions (breath-held GRE) (500 × 320 × 400 mm^3 field of view in the left-right, head-foot, and anterior-posterior dimensions; 4.1 × 2.6 × 3.1 mm^3 resolution; 2-fold parallel imaging acceleration; 19-s acquisition) with subsequent segmentation into 4 tissue classes: air, lung, fat, and soft tissue (with linear attenuation coefficients of 0, 0.0224, 0.0854, and 0.1 cm^{-1}, respectively) (18). This approach was developed largely for oncological indications but has also been evaluated for cardiac PET/MR imaging (19). However, on the basis of our initial experience, we hypothesized that when imaging the heart, breath-held imaging, even at end-expiration, does not accurately correspond to the time-averaged location of the heart during free-breathing PET acquisitions and that this results in mismatch between the PET emission and attenuation data and the potential for image artifacts. Our proposed solution was a free-breathing, 3-dimensional, golden-angle radial, spoiled GRE acquisition (free-breathing radial GRE). Free breathing over the 6- to 7-min acquisition provides a robust representation of the average position of the anatomy in the PET data. Radial acquisition oversamples low spatial frequency data at the center of k-space and with robust reconstruction of moving anatomy from the golden-angle distribution (20,21) provides artifact-free images of the average cardiac location. The image parameters were as follows: 500 × 500 mm^2 coronal field of view, 72 to 88 slices covering the whole body with partial Fourier Cartesian slice encoding, 3-mm isotropic resolution, repetition time of 4.5 ms, echo time of 2.45 ms, in-phase echo time, 9° flip angle, and 1,600 radial views (based on Siemens WIP 793F). MR images were reconstructed using a constant-signal array-coil combination and were then segmented on the basis of image intensity into 2 tissue classes: 1) background (air and lung); and 2) soft tissue (soft tissue and fat), with linear attenuation coefficients of 0 and 0.1 cm^{-1}, respectively. To automate segmentation, pixel values were plotted as a histogram. One peak, including pixels in air and lung, was automatically separated from a second, including pixels in soft tissue. The minimum between peaks was the cutoff. Finally, the attenuation map was smoothed with a 2-dimensional 2-mm full-width-at-half-maximum Gaussian filter in the coronal plane to remove any salt-and-pepper errors in the segmentation. In cohort 2, the protocol was the same, with the addition of the free-breathing radial GRE MRAC sequence prior to contrast-enhanced MR angiography.

Number of iterations of PET reconstruction algorithm—In this study, for imaging small hotspots in the coronary arteries (5 to 10 mm), we investigated the effect of increasing the number of iterations of the PET reconstruction, which is expected to increase the contrast of small objects (22). For any hotspots in the coronary arteries that were identified, we compared images after 3 and 6 iterations of the PET reconstruction. The visual appearance of the hotspot was evaluated and quantified using the target-to-background ratio (TBR) (standard uptake values [SUVs] corrected for blood-pool activity). For this comparison, the novel free-breathing radial GRE MRAC method was used.

IMAGE ANALYSIS. MRAC

PET images were evaluated semiquantitatively by consensus of expert readers (2 cardiologists [M.R.D., M.G.T.] and 1 nuclear medicine physician [R.A.]). The readers were shown PET images, reconstructed with either standard breath-held GRE or free-breathing radial GRE MRAC in conjunction with anatomic images. The readers assessed image artifacts by assigning 1 mark for each occurrence of dark or bright artifacts at the liver-lung and heart-lung interfaces or the bronchus. Summation provided an artifact score. Readers were blinded to patient and MRAC type, and image order was randomized.

In a second evaluation, the readers evaluated the coronary PET/MR images after fusion of PET imaging with contrast-enhanced MR angiography. The readers then recorded whether images allowed complete interpretation or whether artifacts limited or precluded interpretation of the tracer uptake in the coronary vessels or aorta. The rating was enumerated as 0, 1, or 2, respectively, providing an interpretability score. Finally the readers recorded the presence and location of increased tracer uptake in the coronary vasculature. As previously reported, coronary uptake was considered positive if an area of increased activity localized to a coronary artery on multiple slices on more than 1 reformatted plane and if the maximal TBR (TBR_{max}) value in this region was >25% higher than a proximal reference coronary segment (8).

Number of iterations—PET images of coronary hotspots reconstructed with either 3 or 6 iterations were shown side by side in a blinded, randomized order to the expert readers, who judged which had preferable signal strength and differentiation from its surroundings. TBR values were calculated by drawing regions of interest around the coronary hotspot and in the blood pool in the pulmonary artery or right atrium. Mean TBR and TBR_{max} values were calculated from the mean and maximal activity in the hotspot divided by the mean activity in the blood pool. The same regions of interest were used to analyze images produced after both 3 and 6 iterations.

STATISTICAL ANALYSIS

Continuous variables are presented as mean ± SD or as median (interquartile range [IQR]) if not normally distributed. The significance of differences between reader ratings and TBR values was determined by a 2-sided ordinal Wilcoxon matched-pairs signed rank test and a 2-tailed paired Student *t* test, respectively (Excel, Microsoft, Redmond, Washington). A p value <0.05 was considered to indicate statistical significance.

RESULTS

PATIENTS

Six patients (n = 3 ^{18}F-NaF, n = 3 ^{18}F-FDG) were recruited to cohort 1Seventeen patients (n = 9 ^{18}F-NaF, n = 8 ^{18}F-FDG) were recruited to cohort 2 (**Table 1**). Patients imaged with ^{18}F-FDG had less advanced atherosclerosis than patients imaged with ^{18}F-NaF. The average administered dose of ^{18}F-NaF was 386 ± 78 MBq, and the average dose for ^{18}F-FDG was 412 ± 81 MBq. Effective suppression of myocardial ^{18}F-FDG uptake was achieved in 2 patients (25%). In the remaining 6 patients, there was some degree of physiological uptake, limiting the assessment of true coronary activity.

INITIAL EXPERIENCE

In cohort 1, we noted major PET image artifacts at the diaphragm, at the heart-lung interface, and in the bronchi that generated unphysiologically high and low signal in the majority of patients. This limited evaluation of PET activity in the coronary arteries and aorta (**Figure 1**). This pattern was seen using both ^{18}F-NaF and ^{18}F-FDG radiotracers. The appearance of the artifacts was reminiscent of artifacts at the diaphragm arising from mismatch of the PET emission and attenuation data because of respiratory motion, which has been previously noted on both PET/CT and PET/MR imaging (23,24). The need for matching attenuation and PET data has also been previously described for cardiac PET/MR imaging (25). In addition, we observed that the bronchi were not segmented from the surrounding structures in the attenuation maps produced by the standard MR imaging protocol (**Figure 1**).

QUALITATIVE EVALUATION

In cohort 2, the free-breathing radial GRE MRAC acquisition was robust in all patients. No radial artifacts were observed in the radial GRE images. Automatic segmentation into soft tissue and air was straightforward and correctly identified the bronchus. This removed the artificially high PET signal in the bronchus, improving the interpretability of PET uptake in the aorta and coronary arteries compared with PET images reconstructed using the standard approach. Furthermore, when aligned with PET images, the locations of the liver-lung and heart-lung boundaries on free-breathing radial GRE MRAC closely matched those seen on PET images. The resulting PET images showed no discernible artifacts at these anatomic boundaries (**Figure 2**). Similar results were obtained for both ^{18}F-NaF and ^{18}F-FDG PET images.

Using the standard breath-held GRE MRAC approach, ^{18}F-NaF uptake was observed in 1 vessel segment in the left anterior descending coronary artery (LAD). Using the novel free-breathing radial GRE MRAC approach, a total of 7 hotspots of increased coronary ^{18}F-NaF tracer uptake were identified in 4 patients. All were male, with an average age of 63.5 years. Three had stable coronary artery disease, 1 of whom had a percutaneous coronary intervention in a vessel remote from the observed uptake 2 days prior to imaging and was on statin therapy. One patient had unstable disease, being 6 months post–myocardial infarction for which he did not undergo revascularization. He reported post-infarct angina, hypertension, and hyperlipidemia and was on a statin.

Hotspots were distributed across all 3 coronary vessels: 3 in the LAD, left circumflex coronary artery, and 3 in the right coronary artery. In the patient with recent myocardial infarction, ^{18}F-NaF uptake was observed in the culprit LAD plaque, while late gadolinium enhancement images confirmed that he had sustained a transmural anterior myocardial infarction in the distribution of that lesion (**Figure 3**). Two other examples are shown in **Figure 4**, including 1 in the LAD and 1 at the ostium of the right coronary artery. In both cases the plaques were identified when using the novel free-breathing MRAC but were ambiguous or absent when using the standard breath-held approach. Among patients imaged with ^{18}F-FDG, there was only 1 coronary lesion that appeared to demonstrate increased PET uptake in the LAD (**Figure 4**).

QUANTITATIVE EVALUATION

In evaluation 1, PET images with free-breathing radial GRE MRAC were less affected by artifacts than with standard breath-held GRE. The average artifact scores for free-breathing radial GRE and breath-held GRE MRAC were 0 (IQR: 0 to 0) and 3 (IQR: 2 to 3), respectively ($p < 0.001$). In evaluation 2, PET images of the coronary vessel and aorta were more interpretable with the novel free-breathing radial GRE MRAC compared with breath-held GRE. Using the standard breath-held GRE MRAC, only 1 of the 17 scans was completely interpretable in all coronary territories, and 1 scan was completely noninterpretable, while in 15 patients, at least 1 coronary territory was deemed noninterpretable. By contrast, with the novel free-breathing radial GRE MRAC, 16 of 17 images were completely interpretable. Average interpretability scores for the coronary arteries and aorta using free-breathing radial GRE MRAC were 0 (IQR: 0 to 0) and 0 (IQR:

0 to 0), while for breath-held GRE they were 1 (IQR: 1 to 1) and 1 (IQR: 1 to 1), respectively ($p < 0.001$) (Table 2).

NUMBER OF ITERATIONS IN PET RECONSTRUCTION

In the 7 coronary lesions identified with ^{18}F-NaF, maximal SUV (SUV_{max}) and TBR_{max} values were significantly higher in images reconstructed with 6 compared with 3 iterations (SUV_{max} 1.22 ± 0.25 vs. 1.05 ± 0.35, $p = 0.009$; TBR_{max} 1.55 ± 0.37 vs. 1.31 ± 0.25, $p = 0.01$). Similarly, for the coronary hotspot identified with ^{18}F-FDG, values were higher with 6 compared with 3 iterations (SUV_{max} 1.24 vs. 1.17 and TBR_{max} 1.61 vs. 1.51). Qualitative assessment showed unanimous preference for 6 iterations, noting greater contrast of the plaque against the surrounding blood pool and myocardium, despite the small increase in noise observed, which is anticipated with more iterations (26).

DISCUSSION

We have demonstrated for the first time that PET/MR imaging of the coronary arteries is feasible using both ^{18}F-FDG and ^{18}F-NaF. However standard methods for attenuation correction resulted in major artifacts from mismatched PET and attenuation correction data, limiting image interpretability in 16 of 17 cases. We have proposed a novel approach to MR-based attenuation correction of PET data using a readily available free-breathing radial GRE MR sequence that eliminates this artifact. Hybrid coronary PET/MR image quality can be further enhanced using 6 rather than 3 iterations of the PET reconstruction. We believe that these simple steps, which add only 5 to 7 min to the overall protocol, are mandatory for future PET/MR studies in coronary atherosclerosis and indeed more generally in the heart.

PET/CT imaging is increasingly being used to image the cardiovascular system, including the heart and vasculature (1,5,6,13,27). The ability to measure disease activity, both inflammation and calcification, in the coronary arteries is particularly appealing with potential to identify patients with active atheroma at increased risk for future cardiovascular events (28). However, this approach is somewhat limited, principally by the combined radiation doses and the effects of cardiac motion. The advent of cardiac PET/MR imaging is therefore of great interest. In this study, the average effective radiation dose was 6.6 mSv for ^{18}F-NaF scans and 7.8 mSv for ^{18}F-FDG scans (29,30). This radiation exposure is up to 50% lower than similar recently reported PET/CT studies, in which the average dose was 13.7 mSv (8,31). Although CT doses are likely to reduce in the future, there is also clear potential to reduce PET/MR doses yet further (to 3 to 4 mSv) using the lower tracer doses described in those studies (8,31) and using sensitive PET/MR systems with time-of-flight PET detectors. Despite the advances in low-dose and cardiac-gated CT imaging, the use of MR rather than CT imaging ensures that the only radiation exposure involved is that associated with administration of the radiotracer. This additional reduction opens up the possibility for multi–time point studies investigating changes in disease activity with time and therapeutic intervention, which would be desirable in chronic conditions such as atherosclerosis. An additional potential benefit of using radiation-free MR imaging is the ability to acquire extensive time-resolved anatomic images that can estimate cardiac motion and be used to correct for motion in the PET data. Moreover, PET/MR imaging offers a wealth of complementary information about plaque characteristics (e.g., hemorrhage and remodeling), myocardial function, perfusion, and the presence of scar related to previous infarction (14). Each of these parameters is known to be of both diagnostic and prognostic value and in combination offer a comprehensive, multifaceted assessment of patients with ischemic heart disease. Although coronary MR angiography is not as accurate as coronary CT angiography, recent advances now provide robust assessments of the proximal and midcoronary vessels (32). We have demonstrated that localization of increased PET activity to these regions is possible on fused coronary PET/MR angiographic data, confirming the exciting potential of this imaging approach.

STUDY LIMITATIONS

There were a number of limitations to this study. First, we would like to investigate our technique in a larger cohort of patients to confirm these initial findings. In particular we would like to validate the PET/MR signal against other atherosclerotic biomarkers, including PET/CT imaging, and to corroborate the extensive validation already provided for both ^{18}F-NaF and ^{18}F-FDG (5,7,8,33). Moreover, we will validate the PET image quality and quantification in comparison with PET/CT imaging.

Second, our novel approach includes only 2 tissue classes, soft tissue and background air, in the attenuation correction. Inclusion of more tissue classes will improve the accuracy of tracer activity quantification (34). Inclusion of bone may be significant in vascular PET/MR imaging, in which the aorta and carotid vessels lie close to the spine.

Third, there was no evaluation of cardiac gating, which is frequently included in PET/CT protocols. In some cases it was apparent that the right coronary artery signal in particular was somewhat blurred, likely the result of cardiac motion.

Finally, it was noted that in 75% of cases (6 of 8), some degree of background ^{18}F-FDG uptake in the myocardium hampered evaluation of ^{18}F-FDG uptake in 1 or more coronary territory. Further work is required to investigate novel methods to suppress myocardial ^{18}F-FDG uptake and to develop more specific radiotracers for inflammation (35).

CONCLUSIONS

We provide the first description of successful PET/MR imaging of the coronary arteries. We highlight that specialized approaches tailored to coronary imaging for both attenuation correction and PET image reconstruction are required. This technique can be used to measure both coronary inflammation and microcalcification at low radiation dose and holds promise in identifying patients with increased atherosclerotic disease activity that may benefit from aggressive risk factor modification.

Acknowledgments

This work was supported by National Institutes of Health grant NIH/NHLBI R01HL071021 (Dr. Fayad) and by the British Heart Foundation FS/14/78/31020 (Dr. Dweck). Dr. Dweck is the 2015 recipient of the Sir Jules Thorn Award for Biomedical Research.

ABBREVIATIONS AND ACRONYMS

CT	computed tomography
^{18}F-FDG	^{18}F-fluorodeoxyglucose
^{18}F-NaF	^{18}F-sodium fluoride
GRE	gradient-recalled echo
IQR	interquartile range
LAD	left anterior descending coronary artery
MR	magnetic resonance
MRAC	magnetic resonance attenuation correction
PET	positron emission tomography
SUV	standard uptake value
TBR	target-to-background ratio

REFERENCES

1. Chin CWL, Pawade TA, Newby DE, Dweck MR. Risk stratification in patients with aortic stenosis using novel imaging approaches. Circ Cardiovasc Imaging. 2015; 8:e003421. [PubMed: 26198161]
2. Dweck MR, Boon NA, Newby DE. Calcific aortic stenosis: a disease of the valve and the myocardium. J Am Coll Cardiol. 2012; 60:1854–63. [PubMed: 23062541]
3. Rudd JHF, Warburton EA, Fryer TD, et al. Imaging atherosclerotic plaque inflammation with [^{18}F]-fluorodeoxyglucose positron emission tomography. Circulation. 2002; 105:2708–11. [PubMed: 12057982]
4. Rudd JHF, Narula J, Strauss HW, et al. Imaging atherosclerotic plaque inflammation by fluorodeoxyglucose with positron emission tomography: ready for prime time? J Am Coll Cardiol. 2010; 55:2527–35. [PubMed: 20513592]
5. Rogers IS, Nasir K, Figueroa AL, et al. Feasibility of FDG imaging of the coronary arteries: comparison between acute coronary syndrome and stable angina. J Am Coll Cardiol Img. 2010; 3:388–97.
6. Dweck MR, Chow MWL, Joshi NV, et al. Coronary arterial ^{18}F-sodium fluoride uptake: a novel marker of plaque biology. J Am Coll Cardiol. 2012; 59:1539–48. [PubMed: 22516444]
7. Irkle A, Vesey AT, Lewis DY, et al. Identifying active vascular microcalcification by (18)F-sodium fluoride positron emission tomography. Nat Commun. 2015; 6:7495. [PubMed: 26151378]
8. Joshi NV, Vesey AT, Williams MC, et al. ^{18}F-fluoride positron emission tomography for identification of ruptured and high-risk coronary atherosclerotic plaques: a prospective clinical trial. Lancet. 2014; 383:705–13. [PubMed: 24224999]
9. Jung JH, Choi Y, Im KC. PET/MRI: technical challenges and recent advances. Nucl Med Mol Imaging. 2016; 50:3–12. [PubMed: 26941854]
10. Pichler BJ, Wehrl HF, Kolb A, Judenhofer MS. Positron emission tomography/magnetic resonance imaging: the next generation of multimodality imaging? Semin Nucl Med. 2008; 38:199–208. [PubMed: 18396179]
11. Ratib O, Nkoulou R. Potential applications of PET/MR imaging in cardiology. J Nucl Med. 2014; 55(Suppl 2):40S–6S. [PubMed: 24762626]

12. Nekolla SG, Martinez-Moeller A, Saraste A. PET and MRI in cardiac imaging: from validation studies to integrated applications. Eur J Nucl Med Mol Imaging. 2009; 36(Suppl 1):S121–30. [PubMed: 19104798]
13. Schneider S, Batrice A, Rischpler C, Eiber M, Ibrahim T, Nekolla SG. Utility of multimodal cardiac imaging with PET/MRI in cardiac sarcoidosis: implications for diagnosis, monitoring and treatment. Eur Heart J. 2014; 35:312. [PubMed: 23975480]
14. Abgral R, Dweck MR, Trivieri MG, et al. Clinical utility of combined FDG-PET/MR to asses myocardial disease. J Am Coll Cardiol Img. Jun 29.2016 [E-pub ahead of print].
15. Hofmann M, Pichler B, Schölkopf B, Beyer T. Towards quantitative PET/MRI: a review of MR-based attenuation correction techniques. Eur J Nucl Med Mol Imaging. 2009; 36(Suppl 1):S93–104. [PubMed: 19104810]
16. Aklan B, Oehmigen M, Beiderwellen K, et al. Impact of point-spread function modeling on PET image quality in integrated PET/MR hybrid imaging. J Nucl Med. 2016; 57:78–84. [PubMed: 26471697]
17. Liu X, Bi X, Huang J, Jerecic R, Carr J, Li D. Contrast-enhanced whole-heart coronary magnetic resonance angiography at 3.0 T: comparison with steady-state free precession technique at 1.5 T. Invest Radiol. 2008; 43:663–8. [PubMed: 18708861]
18. Martinez-Möller A, Souvatzoglou M, Delso G, et al. Tissue classification as a potential approach for attenuation correction in whole-body PET/MRI: evaluation with PET/CT data. J Nucl Med. 2009; 50:520–6. [PubMed: 19289430]
19. Lau JMC, Laforest R, Sotoudeh H, et al. Evaluation ofattenuation correctionincardiacPETusing PET/MR. J Nucl Cardiol. Oct 23.2015 [E-pub ahead of press].
20. Feng L, Grimm R, Block KT, et al. Golden-angle radial sparse parallel MRI: combination of compressed sensing, parallel imaging, and golden-angle radial sampling for fast and flexible dynamic volumetric MRI. Magn Reson Med. 2014; 72:707–17. [PubMed: 24142845]
21. Glover GH, Pauly JM. Projection reconstruction techniques for reduction of motion effects in MRI. Magn Reson Med. 1992; 28:275–89. [PubMed: 1461126]
22. Liow JS, Strother SC. Practical tradeoffs between noise, quantitation, and number of iterations for maximum likelihood-based reconstructions. IEEE Trans Med Imaging. 1991; 10:563–71. [PubMed: 18222862]
23. Beyer T, Antoch G, Müller S, et al. Acquisition protocol considerations for combined PET/CT imaging. J Nucl Med. 2004; 45(Suppl 1):25S–35S. [PubMed: 14736833]
24. Keller SH, Holm S, Hansen AE, et al. Image artifacts from MR-based attenuation correction in clinical, whole-body PET/MRI. Magma. 2013; 26:173–81. [PubMed: 22996323]
25. Ai H, Pan T. Feasibility of using respiration-averaged MR images for attenuation correction of cardiac PET/MR imaging. J Appl Clin Med Phys. 2015; 16:5194.
26. Barrett HH, Wilson DW, Tsui BM. Noise properties of the EM algorithm: I. Theory. Phys Med Biol. 1994; 39:833–46. [PubMed: 15552088]
27. Dweck MR, Doris MK, Motwani M, et al. Imaging of coronary atherosclerosis—evolution towards new treatment strategies. Nat Rev Cardiol. 2016; 13:533–48. [PubMed: 27226154]
28. Dweck MR, Aikawa E, Newby DE, et al. Noninvasive molecular imaging of disease activity in atherosclerosis. Circ Res. 2016; 119:330–40. [PubMed: 27390335]
29. International Commission on Radiological Protection. Radiation dose to patients from radiopharmaceuticals. Addendum 3 to ICRP Publication 53. ICRP Publication No. 106. Ann ICRP. 2008; 38:1–197. [PubMed: 19154964]
30. Kurdziel KA, Shih JH, Apolo AB, et al. The kinetics and reproducibility of ^{18}F-sodium fluoride for oncology using current PET camera technology. J Nucl Med. 2012; 53:1175–84. [PubMed: 22728263]
31. Rubeaux M, Joshi NV, Dweck MR, et al. Motion correction of ^{18}F-NaF PET for imaging coronary atherosclerotic plaques. J Nucl Med. 2016; 57:54–9. [PubMed: 26471691]
32. Dweck MR, Puntman V, Vesey AT, Fayad ZA, Nagel E. MR imaging of coronary arteries and plaques. J Am Coll Cardiol Img. 2016; 9:306–16.

33. Tawakol A, Migrino RQ, Bashian GG, et al. In vivo ^{18}F-fluorodeoxyglucose positron emission tomography imaging provides a noninvasive measure of carotid plaque inflammation in patients. J Am Coll Cardiol. 2006; 48:1818–24. [PubMed: 17084256]
34. Karakatsanis N, Robson P, Dweck M, et al. MR-based attenuation correction in cardiovascular PET/MR imaging: challenges and practical solutions for cardiorespiratory motion and tissue class segmentation. J Nucl Med. 2016; 57(Suppl 2):452.
35. Tarkin JM, Joshi FR, Rudd JHF. PET imaging of inflammation in atherosclerosis. Nat Rev Cardiol. 2014; 11:443–57. [PubMed: 24913061]

PERSPECTIVES

COMPETENCY IN PATIENT CARE AND PROCEDURAL SKILLS: Hybrid PET/MR imaging of atherosclerotic inflammation (^{18}F-FDG) and microcalcification (^{18}F-NaF) in the coronary arteries is feasible. Combined PET/MR imaging allows the depiction of disease activity at low radiation dose, potentially enabling serial imaging of vascular disease activity in both the clinical and research arenas. Moreover, PET/MR imaging combines disease activity measurements with anatomic data, functional assessments, and soft tissue characterization provided by MR in a single scan.

TRANSLATIONAL OUTLOOK: Further studies are now required to confirm our initial findings. Additional technical developments in the areas of attenuation correction and motion correction will continue to improve coronary PET/MR imaging and tracer uptake quantification, resulting in further advances in the assessment of atherosclerotic disease activity.

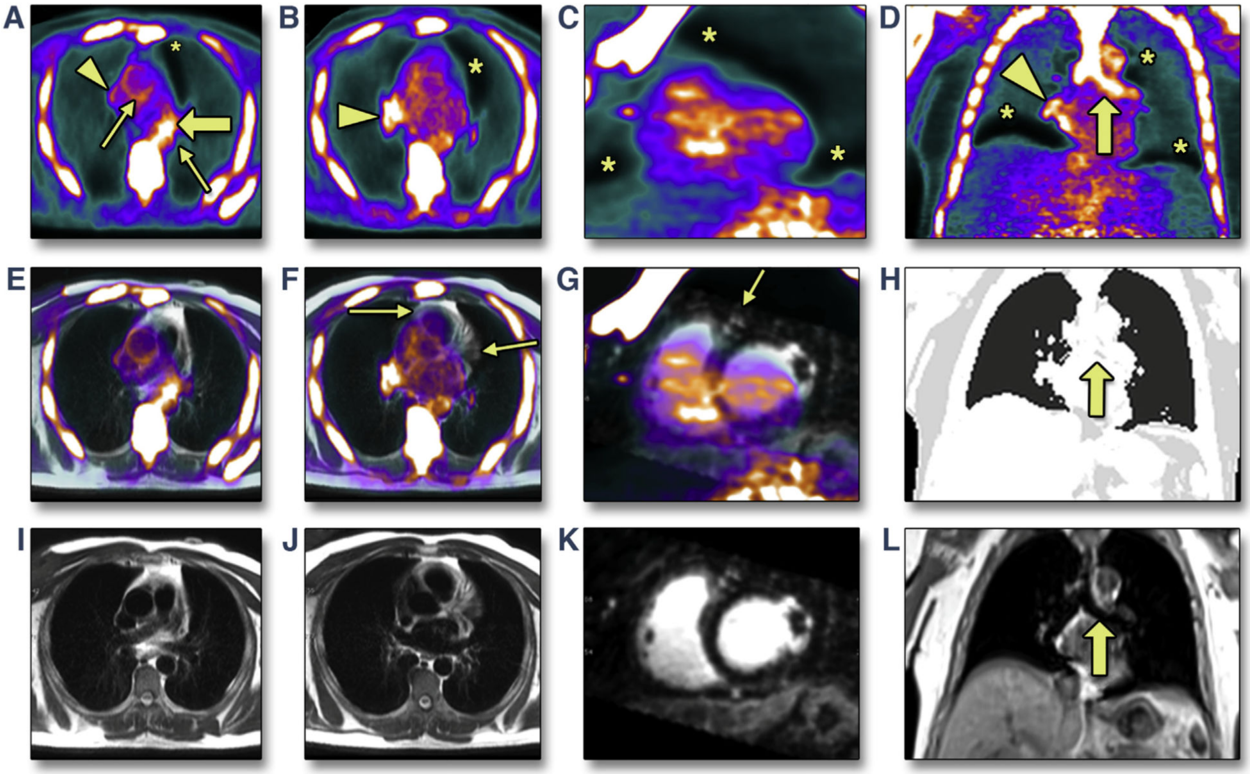

FIGURE 1. Artifacts on Positron Emission Tomographic/Magnetic Resonance Images of the Heart With Standard Methods for Attenuation Correction

Initial experience revealed that ^{18}F-sodium fluoride positron emission tomographic (PET) images reconstructed using standard breath-held gradient-recalled echo (GRE) magnetic resonance attenuation correction **(A to D)** show artifacts that interfere with the assessment of uptake in the aorta and coronary arteries seen on fused PET/magnetic resonance (MR) **(E to G)** and on MR (attenuation map **[H]**, axial single-shot turbo spin echo **[I,J]**, reformatted short-axis 3-dimensional MR angiography **[K]**, and coronal GRE **[L]**). A standard attenuation map **(H)** does not segment the bronchus **(solid arrow)**, which is clearly visible in the corresponding breath-held GRE source image **(L)**. Typical artifacts seen include underestimation of uptake at liver-lung and heart-lung boundaries **(asterisk)**, overestimation at heart-lung boundaries **(arrowhead)**, and bright artifacts in the bronchus **(solid arrow)**. **Arrows** show bronchus and edge artifact, limiting assessment of the ascending and descending aorta **(A)**; heart-lung boundary underestimation coinciding with the courses of the left and right coronary arteries **(F)**; and, in the short-axis view, the left anterior descending coronary artery falling within the heart-lung boundary underestimation artifact **(G)**.

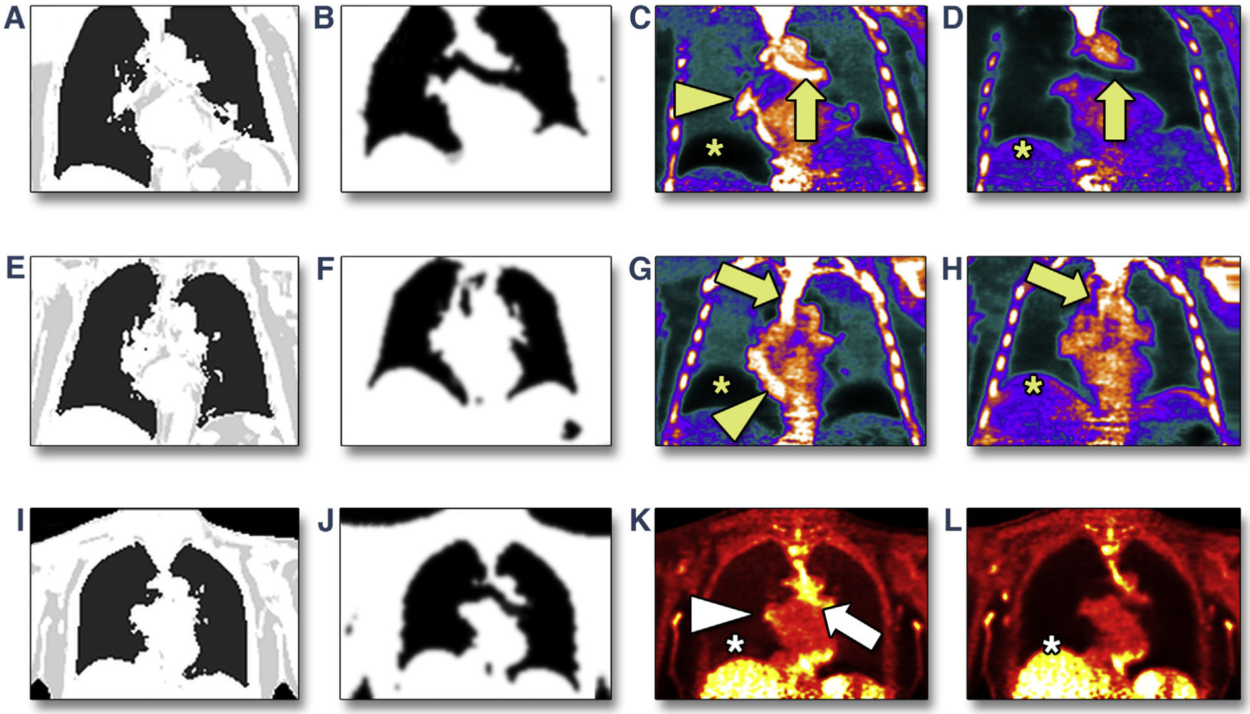

FIGURE 2. Resolution of Positron Emission Tomographic/Magnetic Resonance Artifacts Using the Novel Free-Breathing Radial Gradient-Recalled Echo Attenuation Correction Approach

In 2 patients undergoing ^{18}F-sodium fluoride positron emission tomographic (PET) imaging **(A to D, E to H)** and 1 undergoing ^{18}F-fluorodeoxyglucose PET imaging **(I–L)**, attenuation maps were based either on standard breath-held gradient-recalled echo (GRE) **(A, E, I)** or free-breathing radial GRE **(B, F, J)**. Artifacts at the liver-lung and heart-lung boundaries and in the bronchus present in PET images reconstructed with breath-held GRE magnetic resonance attenuation correction (MRAC) **(C, G, K)** are removed by using the novel free-breathing radial GRE approach for MRAC **(D, H, L)**.

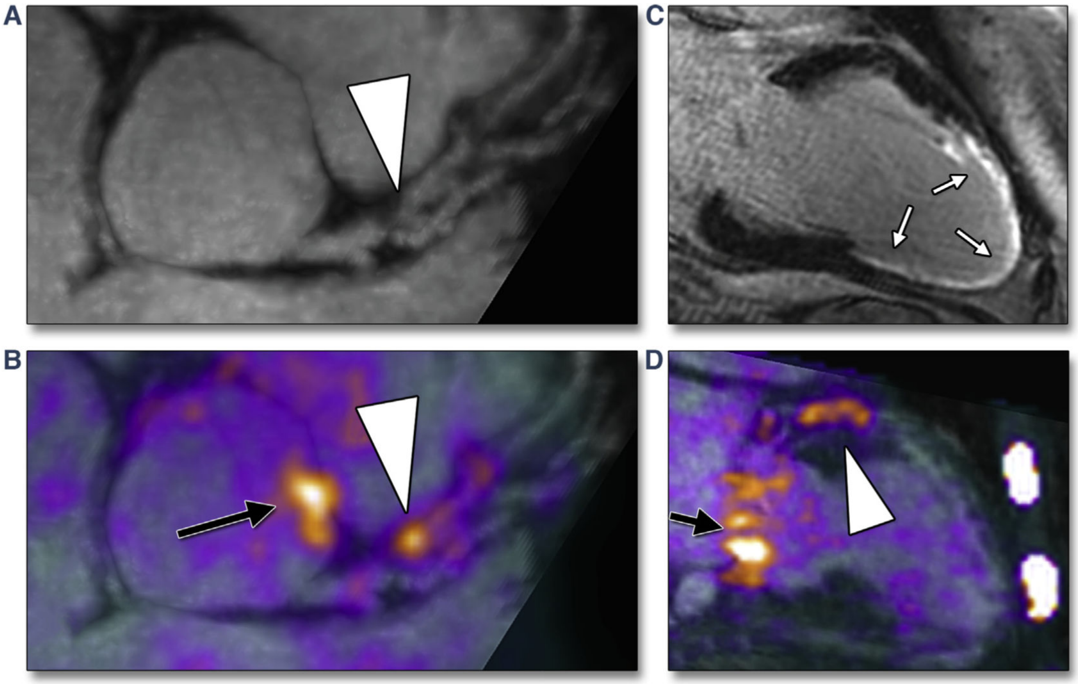

FIGURE 3. Examples of Increased Coronary ^{18}F-Sodium Fluoride Uptake on Positron Emission Tomographic/Magnetic Resonance Images

Reformatted views of a culprit plaque in the left anterior descending coronary artery (LAD) of patient #12, who was 6 months post–myocardial infarction: plaque **(arrowhead)** is observed, causing a proximal luminal stenosis on magnetic resonance (MR) angiography **(A)**. Increased ^{18}F-sodium fluoride (NaF) uptake is observed at exactly this site on fused positron emission tomographic (PET)/MR images **(B, arrowhead)**. An extensive near-transmural myocardial infarction is confirmed on late gadolinium enhancement images corresponding to the perfusion territory of this lesion **(white arrows) (C)**. Elevated ^{18}F-NaF uptake is again observed in the culprit lesion in the LAD on a 2-chamber view of the left ventricle **(arrowhead, D)**. Also note increased uptake in the aortic root **(black arrow, B)** and in the mitral valve annulus **(black arrow, D)**. All images were acquired during a single PET/MR scan.

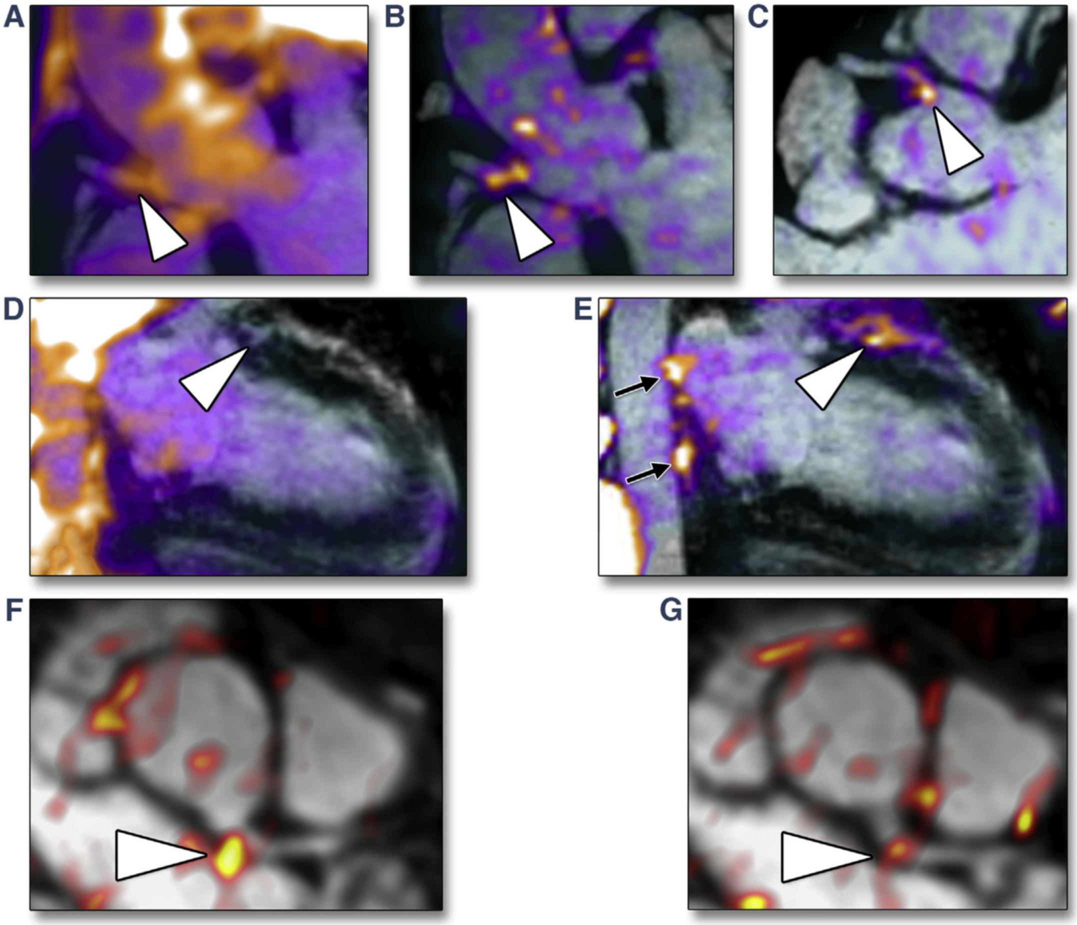

FIGURE 4. Further Examples of Increased Coronary ^{18}F-Sodium Fluoride and ^{18}F-Fluorodeoxyglucose Uptake on Fused Coronary Positron Emission Tomographic/Magnetic Resonance Images

Focal elevation of ^{18}F-sodium fluoride (NaF) signal is seen in the proximal right coronary artery of patient #8, who had stable coronary artery disease (CAD) **(arrowheads, A to C)**. This is ambiguous when reconstructed using standard breath-held gradient-recalled echo (GRE) magnetic resonance attenuation correction (MRAC) **(A)** but is clearly seen on 2 different views when using free-breathing radial GRE MRAC **(B, C)**. In patient #15, who had stable CAD, elevated ^{18}F-NaF signal in the left anterior descending coronary artery **(arrowhead)** and in the thoracic aorta **(short arrows)** is absent when reconstructed with standard breath-held GRE MRAC **(D)** but is clearly identified with free-breathing radial GRE MRAC **(E)**. In patient #6, there is an apparent elevation of the ^{18}F-fluorodeoxyglucose signal in the left main stem observed in 2 adjacent slices **(F, G) (arrowhead)**.

TABLE 1

Patient Demographics

	Cohort 1	**Cohort 2**
Age, yrs	68 (50–67)	54 (31-73)
Sex	3 male, 3 female	11 male, 6 female
Smokers	0	0
BMI, kg/m^2	28 (27–35)	27 (20–36)
Systolic blood pressure, mm Hg	134	127
Hypertension	2	10
Hyperlipidemia	1	4
Diabetes	3	1
Angina	1	2
Previous PCI	1	2
Previous MI	0	1
Administered dose of ^{18}F-NaF/^{18}F-FDG, MBq	453/390	363/420
Effective radiation dose of ^{18}F-NaF/^{18}F-FDG, mSv	7.70/7.41	6.17/7.98

Values are mean (range) or n.

BMI = body mass index; FDG = fluorodeoxyglucose; MI = myocardial infarction; NaF = sodium fluoride; PCI = percutaneous coronary intervention.

TABLE 2

Summary of Quantitative Evaluations in Cohort 2

	Artifact Score MRAC Type		Interpretability Score MRAC Type				Uptake Evaluation MRAC Type	
			Breath-Held GRE		Free-Breathing Radial GRE			
Patient #	**Breath-Held GRE**	**Free-Breathing Radial GRE**	**Coronary**	**Aorta**	**Coronary**	**Aorta**	**Breath-Held GRE**	**Free-Breathing Radial GRE**
1	4	0	1	1	0	0	—	—
2	0	1	0	0	0	0	—	—
3	2	0	1	1	0	0	—	—
4	4	0	1	1	0	0	—	RCA
5	3	0	1	1	0	0	—	—
6	3	0	1	1	0	0	—	LAD
7	2	0	1	1	0	0	—	—
8	3	1	1	1	0	0	—	RCA
9	2	0	2	2	2	2	—	—
10	3	0	1	1	0	0	—	—
11	1	0	1	1	0	0	—	—
12	4	0	1	1	0	0	LAD	LAD, LCx
13	3	0	1	1	0	0	—	—
14	3	0	1	1	0	0	—	—
15	4	0	1	1	0	0	—	LAD, RCA
16	3	0	1	1	0	0	—	—
17	3	0	1	1	0	0	—	—
Average (mean) (median, interquartile range)	2.76 (3, 2–3)	0.12 (0, 0–0)	1 (1, 1–1)	1 (1, 1–1)	0.12 (0, 0–0)	0.12 (0, 0–0)		

The artifact score was the summation of reader-assigned marks for each artifact observed in positron emission tomographic images reconstructed with either breath-held or free-breathing MRAC. The interpretability score was the enumeration of readers' evaluations of the interpretability of radiotracer uptake in the coronary arteries and aorta. For uptake evaluation, readers recorded vessels in which focal radiotracer uptake was identified.

GRE = gradient-recalled echo; LAD = left anterior descending coronary artery; LCx = left circumflex coronary artery; MRAC = magnetic resonance attenuation correction; RCA = right coronary artery.